

Influence of one specific carbon–carbon bond on the quality, stability, and photovoltaic performance of hybrid organic–inorganic bismuth–iodide materials

David M. Fabian[†], Alex M. Ganose^{‡†L}, Joseph W. Ziller[†], David O. Scanlon^{‡†L}, Matthew C. Beard^{}, and Shane Ardo^{*†Δ}*

[†]Department of Chemistry, University of California Irvine, Irvine, CA 92697-2025, United States

[‡]Department of Chemistry, University College London, 20 Gordon Street, London WC1H 0AJ, United Kingdom

^LDiamond Light Source, Harwell Campus, Didcot OX11 0DE, United Kingdom

^LThomas Young Centre, University College London, Gower Street, London WC1E 6BT, United Kingdom

^{*}National Renewable Energy Laboratory, Golden, Colorado 80401, United States

^ΔDepartment of Chemical Engineering and Materials Science, University of California Irvine, Irvine, CA 92697-2025, United States

KEYWORDS: bismuth–halide, hybrid organic–inorganic, dications, stability, non-toxic, photovoltaic, solar cells, solar fuels

ABSTRACT: Hybrid organic–inorganic halide perovskites are promising thin-film solar cell materials. However, the toxicity and instability of champion lead–halide perovskite materials make them non-ideal. To combat these issues, we replaced lead with bismuth and explored the sensitivity of these new lead-free materials to the valency and bonding of their cationic organic groups. Specifically, we synthesized and characterized the materials properties and photophysical properties of hexanediammonium bismuth pentaiodide ((HDA²⁺)BiI₅) and compared them to an analog containing a more volatile organic group with half the number of carbon and nitrogen atoms in the form of propylammonium ((PA⁺)_xBiI_y). The full crystallographic structures of (HDA²⁺)BiI₅ and (PA⁺)_xBiI_y were resolved by single-crystal X-ray diffraction. (HDA²⁺)BiI₅ was shown to be pure-phase and have a one-dimensional structure, whereas (PA⁺)_xBiI_y was shown to be a mix of one-dimensional and zero-dimensional phases. Structures of the materials were confirmed by synchrotron X-ray diffraction of powders. Both (HDA²⁺)BiI₅ and (PA⁺)_xBiI_y exhibit steady-state photoluminescence at room temperature, indicative of high materials quality. Density functional theory calculations of (HDA²⁺)BiI₅ predict electronic absorption features and a ~2 eV bandgap that are consistent with those observed experimentally. Structure–property relationships of the materials were examined, and moisture tolerance and film quality were found to be superior for dication-containing (HDA²⁺)BiI₅ in relation to monocation-containing (PA⁺)_xBiI_y. We hypothesize that these trends are in part due to a molecular bridging effect enabled by the presence of the dicationic hexanediammonium groups in (HDA²⁺)BiI₅. Solar cells fabricated using (HDA²⁺)BiI₅ as the photoactive layer exhibited photovoltaic action while those containing (PA⁺)_xBiI_y did not, suggesting that organic dicationic groups are beneficial to light-absorber morphology and ultimately solar cell performance.

INTRODUCTION

Lead-halide-based hybrid organic-inorganic perovskite materials (APbX₃) are promising light-absorbers for use in thin-film solar cells due to their low-temperature processability¹⁻³ and demonstrated laboratory-scale efficiencies of > 20%.^{4,5} APbX₃ has also been incorporated in devices for solar fuels production, where solar-to-hydrogen conversion efficiencies of 2.5% have been reported.^{6,7} While application of this new materials class in solar fuels devices may lead to a promising technology, APbX₃ is not ideal because it contains toxic lead and the materials are unstable in humid ambient conditions. Compatibility with humid air is the minimum requirement for a solar fuels device that uses water as a clean source of electrons.⁸⁻¹⁰ Therefore, research into classes of photoactive materials that are moisture tolerant and are of a high quality is important.

We have previously reported a one-dimensional perovskite-like bismuth-halide material, hexanediammonium bismuth pentaiodide, NH₃(CH₃)₆NH₃BiI₅ ((HDA²⁺)BiI₅), for use as the photoactive layer in solar cells.¹¹ When processed under ambient conditions, this material exhibited superior film quality, photovoltaic performance, and stability in comparison to the widely-studied three-dimensional methylammonium lead triiodide. We proposed that the dicationic nature of the organic hexanediammonium groups allowed it to bridge unit cells in the structure and provide increased stability. Evidence for this structural arrangement is supported by single-crystal X-ray structures of these materials reported by Mousdis et al.¹² While some additional studies have been performed using these materials,^{13,14} no additional evidence exists that this structural architecture provides increased stability. To further assess this, herein we compare one-dimensional ((HDA²⁺)BiI₅), which contains bridging dicationic organic groups, to an analog that contains only non-bridging monocationic organic propylammonium (PA⁺) groups with half the number of carbon and nitrogen atoms.

In 2000, Mitzi introduced the possibility of using non-toxic lower-dimensional photoactive materials in hybrid organic–inorganic solar cells with introduction of metal-deficient two-dimensional $(\text{H}_2\text{AEQT})\text{Bi}_2\text{I}_4$, where $\text{AEQT} = 5,5''\text{-bis-(aminoethyl)-2,2':5',2'':5'',2''\text{-quaterthiophene}$.¹⁵ Since then only two other analogous two-dimensional bismuth-containing materials have been reported: $(\text{NH}_4)_3\text{Bi}_2\text{I}_9$,¹⁶ and $(\text{TMP})_{1.5}[\text{Bi}_2\text{I}_7\text{Cl}_2]$, where $\text{TMP} = N,N,N',N'$ -tetramethylpiperazine.¹⁷ The all-inorganic analog, bismuth iodide (BiI_3), also exhibits a two-dimensional layered structure of BiI_6^{3-} octahedra and has been incorporated in solar cells with efficiencies as high as 1.2%.^{18–20} Other hybrid bismuth–halide photoactive layers that have been used in solar cells primarily fall into the class of zero-dimensional $\text{A}_3\text{Bi}_2\text{I}_9$ materials, where $\text{A} = \text{K}^+, \text{Rb}^+, \text{Cs}^+$, methylammonium, or formamidinium, and from which solar cell efficiencies up to 1.64% have been achieved.^{21–25} The low dimensionality of the binuclear clusters of zero-dimensional octahedra results in low charge conductivity^{16,26–30} and therefore, it is speculated that the charge-carrier diffusion lengths are much smaller than those measured for hybrid organic–inorganic materials of higher dimensionality.

While our study will help assess whether specific dicationic organic groups are advantageous to materials properties and moisture stability in this class of hybrid organic–inorganic materials, this comparison is only possible in lower-dimensional materials due to charge balancing. Three-dimensional hybrid organic–inorganic analogs only require single cations per unit cell, yet they often result in more efficient solar cell performance due to the three-dimensional connectivity of the inorganic units, which facilitate charge-carrier conduction.³¹ When the dimensionality of the materials is reduced from three, the inorganic units become much more electronically isolated from each other, resulting in poorer electrical conduction.³² In cases where the electrically-insulating organic unit is small enough, weak electronic interactions between the

inorganic units still exist,³¹ therefore enabling at least moderate conduction and performance. Herein, we report a comparative study using one-dimensional (HDA²⁺)BiI₅ that contains divalent organic cations vs. an analogous (PA⁺)_xBiI_y material that contains monovalent organic cations and half the number of carbon and nitrogen atoms. Structural information of material powders and thin films, theoretical maximum solar cell efficiencies, stability, and photophysical properties are compared in order to elucidate structure–property relationships in these hybrid organic–inorganic bismuth–halide materials.

EXPERIMENTAL SECTION

Single-Crystal Growth. Single crystals of (HDA²⁺)BiI₅ were grown by vapor diffusion of dichloromethane into a 0.5 M solution of 1:1 hexandiamine dihydriodide (HDAI₂):BiI₃, where HDAI₂ in slight excess to ensure there was no residual BiI₃, in a solvent mixture of 4:1 (v/v) *N,N*-dimethylformamide (DMF):dimethylsulfoxide (DMSO). Single crystals of (PA⁺)_xBiI_y were grown by vapor diffusion of dichloromethane into a 0.5 M solution of 2:1 propylamine hydriodide (PAI):BiI₃, with PAI in slight excess to ensure there was no residual BiI₃, in methanol. Details on single-crystal X-ray data collection and structure solutions for (HDA²⁺)BiI₅ and (PA⁺)_xBiI_y are provided in the Supporting Information. Density Functional Theory Calculations for (HDA²⁺)BiI₅ and (PA⁺)_xBiI_y are also provided in the Supporting Information.

Solution Preparation. All chemicals were used as received. Ammonium iodide salts were synthesized by slow addition of hydriodic acid (47% in water, stabilized with 1.5% hypophosphorous acid, Sigma-Aldrich) to either 1,6-hexanediamine (98+%, Alfa Aesar) or propylamine (98%, Sigma-Aldrich) dissolved in methanol. As an example, to synthesize HDAI₂, 260.9 mg of 1,6-hexanediamine was dissolved in 5 mL methanol, and then 1 mL hydriodic acid was added slowly at 0 °C with stirring, followed by stirring for an additional 30 min. In this case,

the hydriodic acid to amine molar ratio was 2:1, with hydriodic acid in slight excess. HDAl₂ precipitate was recovered by evaporation of solvents at 40 °C with a rotary evaporator. The precipitate was rinsed with diethyl ether, and vacuum dried at 60 °C for at least 12 h. An analogous procedure for the preparation of PAI was carried out, but the hydriodic acid to amine molar ratio was 1:1, with hydriodic acid in slight excess. 0.5 M solutions of (HDA²⁺)BiI₅ and (PA⁺)_xBiI_y were then prepared by mixing powders of HDAl₂ or PAI with BiI₃ (99.999%, Sigma-Aldrich) at an approximately 1:1 mole ratio, with HDAl₂ or PAI in slight excess, in an anhydrous mixture of 4:1 (v/v) DMF:DMSO at 70 °C inside a nitrogen-filled glovebox. The (HDA²⁺)BiI₅ and (PA⁺)_xBiI_y solutions were stored in the glovebox until use and were used within one week of preparation.

Materials Processing. All steps of materials deposition and solar cell fabrication were performed in air with 40% – 60% relative humidity and as described below, unless noted otherwise. All thermal treatments were performed using a hot plate. Fluorine-doped tin-oxide coated glass (FTO) substrates were cleaned as follows: 1) sonication in Alconox solution, 2) rinse with deionized water, 3) rinse with ethanol, 4) sonication in ethanol, and 5) dry with nitrogen. A compact TiO₂ (cTiO₂) layer was deposited by pipetting a solution of titanium diisopropoxide bis(acetylacetonate) on a cleaned FTO substrate and then the substrate was spun at 2000 rpm (2000 rpm/s acceleration) for 60 s. The substrate was subsequently dried at 125 °C and then sintered at 550 °C for 30 min. Nanoparticles of TiO₂ were synthesized following a procedure by Ito et al.³³ The nanoparticle solution was further diluted in ethanol at a ratio of 1:3.5 TiO₂ nanoparticle solution:ethanol, w/w to make a mesoporous TiO₂ (mTiO₂) suspension. The mTiO₂ layer was deposited by spin coating this solution at 500 rpm (500 rpm/s acceleration) for 5 s and then 5000 rpm (5000 rpm/s acceleration) for 25 s, followed by drying at 125 °C, and then sintering at 550 °C for 30 min. The substrates were allowed to cool to room temperature. Unless otherwise noted, a conventional spin-

coat method was adapted from Kim et al.³⁴ and used for depositing the hybrid organic–inorganic bismuth–iodide solutions that served as the photoactive layer. For this method, a filtered solution of $(\text{HDA}^{2+})\text{BiI}_5$ or $(\text{PA}^+)_x\text{BiI}_y$ in 4:1 (v/v) DMF:DMSO was pipetted on top of the mTiO_2 -coated FTO substrate and then the substrate was spun at 3000 rpm (3000 rpm/s acceleration) for 60 s, followed by rapid transfer to a hot plate that was preheated to 100 °C and subsequent annealing at 100 °C for 45 min. In some cases, the fast-deposition crystallization method was employed for depositing the photoactive layer, which was adapted from Xiao et al.³⁵ For the fast-deposition crystallization method, the photoactive layer solution was spun at 6000 rpm and 6000 rpm/s acceleration for 30 s total, and 6 s before the end of the spin process, anhydrous chlorobenzene was dispensed onto the film while the substrate was spinning. For both photoactive layer deposition methods, the photoactive layer solution was dispensed on the substrate at a volume of 17.5 $\mu\text{L}/\text{cm}^2$.

Characterization. All samples for characterization were measured under ambient conditions. High-resolution synchrotron powder diffraction data were collected using beamline 11-BM at the Advanced Photon Source at Argonne National Laboratory using a calibrated wavelength of 0.41417 Å. Discrete detectors covering an angular range from -6 to $16^\circ 2\theta$ are scanned over a $34^\circ 2\theta$ range, with data points collected every $0.001^\circ 2\theta$ and scan speed of $0.01^\circ/\text{s}$. Data are collected while continually scanning the diffractometer 2θ arm. A mixture of NIST standard reference materials, Si (SRM 640c) and Al_2O_3 (SRM 676) is used to calibrate the instrument, where the Si lattice constant determines the wavelength for each detector. Corrections are applied for detector sensitivity, 2θ offset, small differences in wavelength between detectors, and the source intensity, as noted by the ion chamber before merging the data into a single set of intensities evenly spaced in 2θ . For ease of data presentation, 2θ values were adjusted as if Cu K_α radiation (1.5406 Å) was

used. Grazing-incidence X-ray diffraction (XRD) data were collected using a Rigaku Smartlab diffractometer with Cu K α radiation and in parallel beam geometry. Scanning electron microscopy (SEM) images were acquired on a FEI Magellan 400L XHR using 15 kV accelerating voltage and 0.8 nA beam current. Thermogravimetric analysis (TGA) data were obtained using a TGA Q500 by TA Instruments. Transmission and reflection spectra were obtained using an integrating sphere in a Shimadzu UV-3600 ultraviolet-visible-near-infrared spectrophotometer. Absorption was calculated by assuming Absorbance = 1 - Transmittance - Reflectance. Steady-state photoluminescence (PL) was measured with a Horiba Jobin Yvon Model FL-1039/40 Fluorolog, a Horiba Jobin Yvon iHR320 spectrograph, and a Horiba Jobin Yvon SPEX Instruments S.A. Group Spectrum One G35 CCD camera. A monochromatized Xe lamp was used as the excitation source. Steady-state PL data were corrected for the wavelength-dependent response of the detection system. Time-resolved photoluminescence spectroscopy measurements were performed using the time-correlated single photon counting technique. Excitation light was generated by a Fianium SC-450-PP laser operating with an average power of 15.5 μ W at a repetition rate of 10 MHz and a wavelength of 450 nm selected by a Fianium AOTF system. A 470 nm long pass filter was used to remove scattering from the excitation source. The emission was detected using a Hamamatsu streak camera with a wavelength range of 200 – 900 nm and response of < 20 ps. For a clearer comparison, data were shifted and normalized so that maximal values of 1 occurred at $t = 0$ ns. To obtain kinetic data, the signal was averaged over the entire spectrum for which there was an appreciable signal (~530 – 700 nm).

RESULTS AND DISCUSSION

Crystals of $(\text{HDA}^{2+})\text{BiI}_5$ grew in the form of red needles and single-crystal XRD data confirmed the crystal structure (Figure 1). These data also provided evidence that the organic dication (white, blue) bridges iodides (green) coordinated to different bismuth(III) ions (yellow) and yielding one-dimensional chains of corner-sharing octahedra.^{11,12} The chains of bismuth-iodide octahedra align perpendicular to the c-axis along the (110) plane, as indicated by the red plane in Figure S1a, which shows a $1 \times 1 \times 3$ unit cell structure of $(\text{HDA}^{2+})\text{BiI}_5$. The organic hexanediammonium groups in the $(\text{HDA}^{2+})\text{BiI}_5$ structure are “c”-shaped, supporting the notion that there is some bonding interaction between terminal ammonium groups of hexanediammonium and iodides of BiI_5^{2-} that is causing the hexanediammonium groups to orient. In Figure S1b, the same structure is displayed but rotated 90° and in Figure S1c the same orientation of the structure as in Figure S1b is displayed, but with the hexanediammonium groups omitted. Figure S1b,c highlight the inorganic BiI_5^{2-} framework of $(\text{HDA}^{2+})\text{BiI}_5$ through which rapid charge-carrier conduction takes place.³⁷ Since the inorganic framework is only one-dimensional, charge-carrier conduction is conjectured to be much faster intra-chain along the c-axis than inter-chain along the a-axis and b-axis. Table S1 shows crystallographic information pertaining to the $(\text{HDA}^{2+})\text{BiI}_5$ single crystal.

We suspected that comparative monocationic $(\text{PA}^+)_x\text{BiI}_y$ crystals would

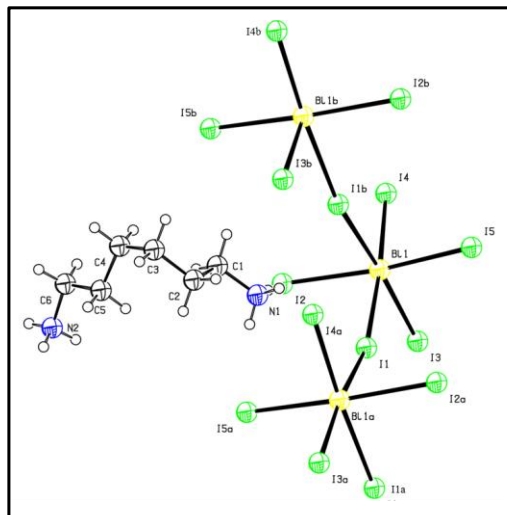


Figure 1. Molecular structure of $(\text{HDA}^{2+})\text{BiI}_5$, with thermal ellipsoids drawn at the 50% probability level and where green = iodine, yellow = bismuth, blue = nitrogen, and white = carbon.

be isostructural to $(\text{HDA}^{2+})\text{BiI}_5$ crystals. However, it is evident from Figure S2 that the inorganic framework of the $(\text{PA}^+)_x\text{BiI}_y$ single crystal is different than that of $(\text{HDA}^{2+})\text{BiI}_5$, because it contains clusters of $\text{Bi}_2\text{I}_9^{3-}$ bioctahedra. This structure is zero-dimensional and therefore, it is much like that of methylammonium bismuth iodide and previously-reported $\text{A}_3\text{Bi}_2\text{I}_9$ materials.^{27,30,38–40} Table S2 shows crystallographic information pertaining to the $(\text{HDA}^{2+})\text{BiI}_5$ single crystal.

Synchrotron XRD was performed on $(\text{HDA}^{2+})\text{BiI}_5$ powders obtained by mechanical abrasion of spin-coated thin films (Figure 2a, red line). The diffraction patterns are consistent with the calculated powder pattern based on the single-crystal data (Figure 2a, black line). The similarity in these diffraction patterns supports that the $(\text{HDA}^{2+})\text{BiI}_5$ single crystal that is seeded from solution has the same structure as the $(\text{HDA}^{2+})\text{BiI}_5$ thin film that crystallizes during annealing. Figure 2b displays the same comparison in XRD patterns for $(\text{PA}^+)_x\text{BiI}_y$. It is evident that other crystal phases are present in the $(\text{PA}^+)_x\text{BiI}_y$ powder scraped off from thin films in addition to the single-crystal phase that grew in solution (Figure S2). In Figure 2b, the peaks labeled in black font correspond to the one-dimensional phase that matches that of $(\text{HDA}^{2+})\text{BiI}_5$ and the peaks labeled

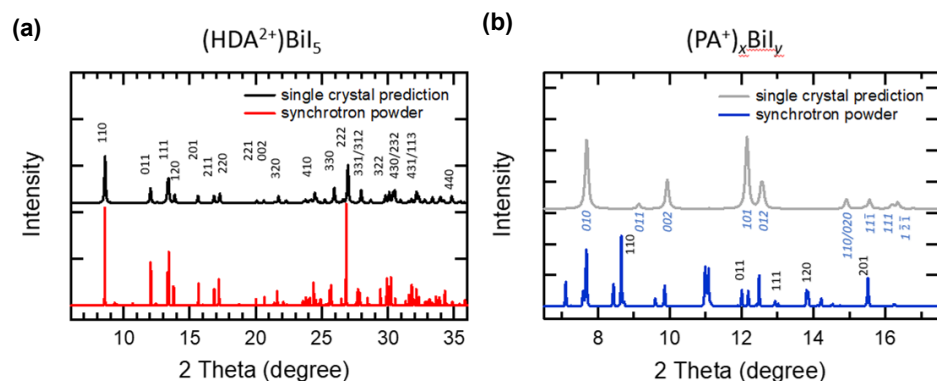


Figure 2. X-ray diffraction patterns of (a) $(\text{HDA}^{2+})\text{BiI}_5$ and (b) $(\text{PA}^+)_x\text{BiI}_y$, measured for powders obtained by mechanical abrasion of spin-coated thin films using a synchrotron source (red and blue lines, respectively) and predicted from the resolved single-crystal structure (black and gray lines, respectively).

Commented [SA1]: Can the caption read “single crystal prediction”

Commented [DF2R1]: Changed

Commented [SA3R1]: Shoot, I meant key; I could change the caption. Whatcha think? Were they predicted from some other data or known?

Commented [DF4R1]: Ah I see. I changed the key. They were predicted using Mercury software from the arrangement of atoms in the resolved crystal structure

Commented [SA5R1]: I think that should be in the Exp Section then as it current isn't, I don't think. Also, I flipped the caption parts around, which is fine, so that the prediction text came second.

Commented [DF6R1]: Added text to the experimental section in the SI.

in blue font correspond to the zero-dimensional phase that matches the resolved single-crystal structure. The unlabeled peaks present in the XRD data presented in Figure 2b are suspected to correspond to a third not-yet-determined phase.

Grazing-incidence XRD data of annealed thin films are presented in Figure 3. The XRD pattern of the $(\text{HDA}^{2+})\text{BiI}_5$ thin film (Figure 3, red line) matches the patterns of the single crystal and powders presented in Figure 2, indicating a phase-pure one-dimensional framework of corner-sharing bismuth-iodide octahedra. For the thin-film XRD pattern of

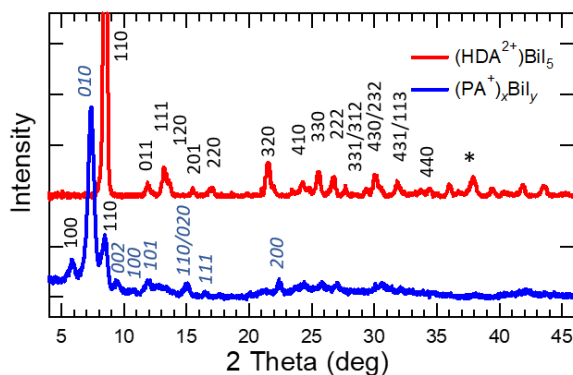


Figure 3. Grazing-incidence X-ray diffraction patterns of thin films of $(\text{HDA}^{2+})\text{BiI}_5$ (red line) and $(\text{PA}^+)_x\text{BiI}_y$ (blue line) thin films on fluorine-doped tin-oxide-coated glass (FTO). The pattern matches well with that obtained for $(\text{HDA}^{2+})\text{BiI}_5/\text{TiO}_2/\text{FTO}$ reported in ref. 1 but $(\text{HDA}^{2+})\text{BiI}_5$ peaks have now been more accurately indexed based on the single-crystal structure determined in Figure 1.

$(\text{PA}^+)_x\text{BiI}_y$ (Figure 3, blue line), however, the dominant peak at $\sim 7.4^\circ$ is indexed to the (200) peak of single-crystal $(\text{PA}^+)_x\text{BiI}_y$, which corresponds to the zero-dimensional phase of the material. It is evident that annealed thin films of $(\text{PA}^+)_x\text{BiI}_y$ contain a mixture of a one-dimensional phase of corner-sharing bismuth-iodide octahedra analogous to $(\text{HDA}^{2+})\text{BiI}_5$ and a zero-dimensional phase containing clusters of bismuth-halide bioctahedra analogous to $\text{A}_3\text{Bi}_2\text{I}_9$ materials.

Density functional theory (DFT) calculations were performed to investigate the optoelectronic properties of $(\text{HDA}^{2+})\text{BiI}_5$ (Figure 4). The HSE06 hybrid functional was employed with spin-orbit coupling effects explicitly included for all calculations. HSE06 has been shown reproduce the lattice parameters and bandgaps of many lead-halide-based and bismuth-halide-

based materials.^{41–43} The indirect and direct bandgaps of $(\text{HDA}^{2+})\text{BiI}_5$ were calculated to be 2.01 eV and 2.03 eV, respectively, in very good agreement with our previously published experimentally measured values of 2.05 eV and 2.15 eV, respectively.¹¹ Inclusion of spin-orbit coupling was found to lower the calculated bandgap of $(\text{HDA}^{2+})\text{BiI}_5$ by 0.68 eV, due to the presence of heavy 6p ions.⁴⁴ The calculated non-parabolic effective masses of the valence-band maximum and conduction-band minimum are smaller for electrons than holes such that they are $0.57 m_0$ at Γ and $2.08 m_0$ at Y for electrons and $0.79 m_0$ at Γ and $5.80 m_0$ at Z for holes, where $m_0 = 9.11 \times 10^{-31}$ kg and is the free electron rest mass.

The calculated optical absorption spectrum of $(\text{HDA}^{2+})\text{BiI}_5$ agrees well with our previously published electronic absorption data,¹¹ in that $(\text{HDA}^{2+})\text{BiI}_5$ shows a similarly large absorption coefficient just above its bandgap (Figure S3). Strong optical absorption is quite surprising for a one-dimensional hybrid organic–inorganic material,⁴⁵ but is beneficial to solar-cell performance. For this reason, we calculated the spectroscopy-limited maximum efficiency (SLME),^{46–48} which

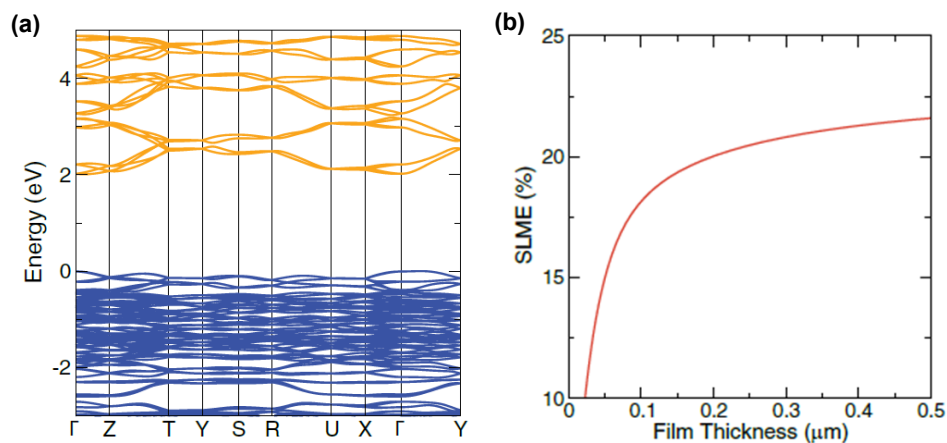


Figure 4. (a) HSE06+SOC band structure of $(\text{HDA}^{2+})\text{BiI}_5$, with the valence-band maximum set equal to 0 eV. (b) Calculated spectroscopy-limited maximum efficiency (SLME) of $(\text{HDA}^{2+})\text{BiI}_5$.

is a metric to predict the maximum solar cell efficiency considering the direct/indirect nature of the bandgap, the strength of optical absorption, and the thickness of the film. For $(\text{HDA}^{2+})\text{BiI}_5$ the efficiency was calculated to be $> 20\%$ for film thicknesses of $> \sim 250$ nm (Figure 4b). This is very close to the Shockley–Queisser detailed-balance limit of 21.6% for a material with a similar bandgap of 2.05 eV and suggests that if the $(\text{HDA}^{2+})\text{BiI}_5$ photoactive layer has a quantum yield for emission of unity and the solar cell has optimal selective contacts, we can approach this efficiency limit.

Electronic absorption and steady-state photoluminescence spectra of thin films of $(\text{HDA}^{2+})\text{BiI}_5$ and $(\text{PA}^+)_{\text{x}}\text{BiI}_y$ are displayed in Figure 5. The more gradual and hypsochromic absorption onset of $(\text{PA}^+)_{\text{x}}\text{BiI}_y$ compared to $(\text{HDA}^{2+})\text{BiI}_5$ supports the XRD data that the $(\text{PA}^+)_{\text{x}}\text{BiI}_y$ film is composed of a mix of one-dimensional and zero-dimensional phases. Near-band-edge photoluminescence is present from both materials

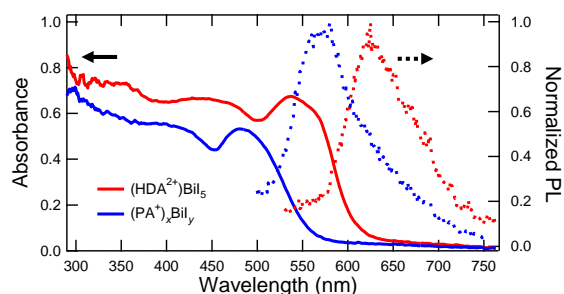


Figure 5. Absorption spectra (solid lines) and steady-state photoluminescence (PL) spectra using excitation at 400 nm (dashed lines) for thin films of $(\text{HDA}^{2+})\text{BiI}_5$ (red lines) and $(\text{PA}^+)_{\text{x}}\text{BiI}_y$ (blue lines).

suggesting that the emission is not from intra-gap trap states.⁴⁹ It is also evident in Figure S4 that there is no wavelength-dependent response to the emission of each film, indicating that the observed signal is not due to a scattering phenomenon.

Time-resolved photoluminescence measurements were carried out on $(\text{HDA}^{2+})\text{BiI}_5$ and $(\text{PA}^+)_{\text{x}}\text{BiI}_y$ thin films. A transient signal above the instrument response was only obtained for the $(\text{HDA}^{2+})\text{BiI}_5$ thin film when 10 wt. % KI was incorporated in the precursor solution, and the

measured photoluminescence lifetime was < 1 ns (Figure S5a). Incorporation of KI was motivated by Stranks et al. who reported that KI healed defects and therefore maximized emission from lead-halide-based perovskite thin films.⁵⁰ Time-resolved photoluminescence spectra of the $(\text{HDA}^{2+})\text{BiI}_5$ thin film with 10 wt. % KI incorporation are shown in Figure S5b. The spectra represent time regions that are prior to signal decay when there is primarily scattering off of the sample (black line), during the majority of the signal decay (green line), and during all of the signal decay out to 0.8 ns (red line). Signals beyond the first scattering time region are predominantly observed in the wavelength range of 625 – 650 nm, which matches the range of maximum steady-state emission intensity.

The determination of an ideal solution deposition method for the hybrid bismuth-iodide materials under investigation was challenging and a single solution-deposition method was not identified that yielded the highest-quality film for each material. This is evident in the (absorbance + reflectance) spectral data presented in Figure S6b, where less scattering at long wavelengths and larger absorbance is desired. Assuming identical thicknesses, values for the absorbance should be the same regardless of deposition method. It is clear, therefore, that reflectance is higher for the $(\text{HDA}^{2+})\text{BiI}_5$ film processed using the fast-deposition crystallization method with chlorobenzene as the antisolvent (red dashed line) than the $(\text{HDA}^{2+})\text{BiI}_5$ film processed by the one-step deposition technique (red solid line). This is evident by the fact that for $(\text{HDA}^{2+})\text{BiI}_5$ film processed using the fast-deposition crystallization method, values of absorbance + reflectance at wavelengths longer than the absorption onset (i.e. $> \sim 625$ nm) are larger than those for the $(\text{HDA}^{2+})\text{BiI}_5$ film processed by the one-step technique. However, the opposite is true for $(\text{PA}^+)_{\text{x}}\text{BiI}_y$ (blue lines). Greater reflectance suggests larger scattering effects of the film that can in part be attributed to poorer film coverage on the substrate.

The disparity in absorption onset and film color can also be explained through differences in thin-film coverage. It is evident from plan-view SEM images of $(\text{HDA}^{2+})\text{BiI}_5$ (Figure S7) and $(\text{PA}^+)_{\text{x}}\text{BiI}_y$ (Figure S7) that even though both material thin films consist of lamellar structures, the surface coverage of $(\text{HDA}^{2+})\text{BiI}_5$ on a TiO_2/FTO substrate is larger than that for $(\text{PA}^+)_{\text{x}}\text{BiI}_y$. The reason for this discrepancy is still unknown, but it is conjectured that the organic dicationic hexanediammonium groups bridge the chains of bismuth-iodide octahedra together more effectively than the organic monocationic propylammonium groups. For a given spin-coat speed, acceleration, and time (3000 rpm, 1 rpm/s acceleration, 60 s) as well as concentration (1 M) in the 4:1 (v/v) DMF:DMSO solution, it is clear that the extent of visible-light absorption by the $(\text{HDA}^{2+})\text{BiI}_5$ thin film is far superior to that by the $(\text{PA}^+)_{\text{x}}\text{BiI}_y$ thin film (Figure S8).

The thermal stability of $(\text{HDA}^{2+})\text{BiI}_5$ and $(\text{PA}^+)_{\text{x}}\text{BiI}_y$ powders were assessed by thermogravimetric analysis (Figure 6). The onset of significant mass loss occurs at a lower temperature for $(\text{PA}^+)_{\text{x}}\text{BiI}_y$ (< 250 °C) than for $(\text{HDA}^{2+})\text{BiI}_5$ (> 300 °C), which is depicted in the derivative plots of Figure 6a (dash-dotted lines). It is also evident in Figure 6a that there is a non-zero slope of the mass loss curve of $(\text{PA}^+)_{\text{x}}\text{BiI}_y$ (blue solid line) even at temperatures below 200

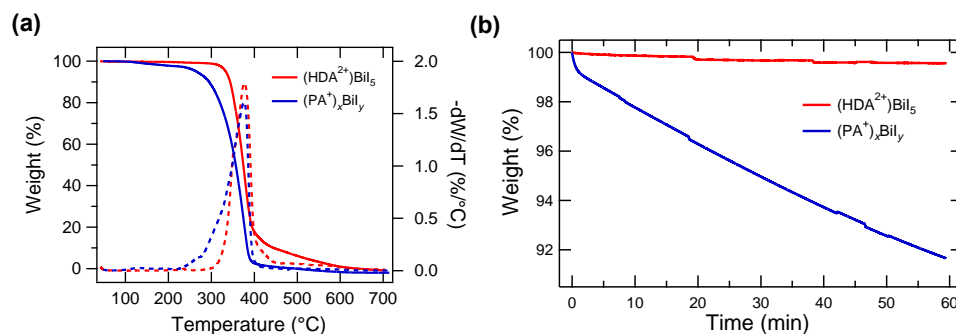


Figure 6. Thermogravimetric analysis of $(\text{HDA}^{2+})\text{BiI}_5$ and $(\text{PA}^+)_{\text{x}}\text{BiI}_y$ powders as a function of (a) temperature at a ramp rate of 20 °C/min and (b) time at 200 °C. In panel a, the solid curves correspond to the % mass remaining (left axis) and the dashed curves correspond to the derivative of the % mass with respect to temperature (right axis).

°C whereas the mass loss curve of (HDA²⁺)BiI₅ is flat (red solid line). This difference is accentuated in the ramp-and-hold thermogravimetric data displayed in Figure 6b, where the temperature in the thermogravimetric chamber was ramped to 200 °C and then held and monitored at 200 °C. After 1 h, the (PA⁺)_xBiI_y powder sample lost ~8% of its original mass whereas the (HDA²⁺)BiI₅ powder sample lost only ~0.5% of its original mass. The greater thermal stability of (HDA²⁺)BiI₅ compared to (PA⁺)_xBiI_y can be rationalized by differences in boiling points of the precursors of the organic groups. The boiling point of hexanediamine is 204 °C and the boiling point of propylamine is 49 °C. In addition, part of the superior stability of (HDA²⁺)BiI₅ could be explained by a molecular bridging effect, where organic dicationic hexanediammonium groups give (HDA²⁺)BiI₅ more structural rigidity than the organic monocationic propylammonium groups do for (PA⁺)_xBiI_y.

Solar cells were fabricated with the architecture Au/spiro-OMeTAD/Bi/mTiO₂/ALD-cTiO₂/FTO, where spiro-OMeTAD is 2,2',7,7'-tetrakis(*N,N'*-di-*p*-methoxyphenylamine)-9,9'-spirobifluorene, Bi is either (HDA²⁺)BiI₅ or (PA⁺)_xBiI_y, and ALD-cTiO₂ is compact TiO₂ deposited via atomic layer deposition. The cTiO₂ layer was deposited by ALD, instead of by solution deposition, because poor solar-cell performance from cells using solution-deposited cTiO₂ was hypothesized to be due to incomplete coverage of the FTO substrate. Current density *versus* voltage (*J-V*) behavior of solar cells with (HDA²⁺)BiI₅ or (PA⁺)_xBiI_y as the photoactive layer and with an ALD-cTiO₂ layer were measured (Figure 7), and the smaller magnitude of the reverse saturation dark current in comparison to using solution-deposited cTiO₂ suggests that the ALD protocol was beneficial.¹¹ Our best-performing solar cell containing (HDA²⁺)BiI₅ had an active area of 0.25 cm² and exhibited an average open-circuit photovoltage (V_{OC}) of > 350 mV, an average short-circuit photocurrent density (J_{SC}) of > 0.18 mA cm⁻², and an average power-

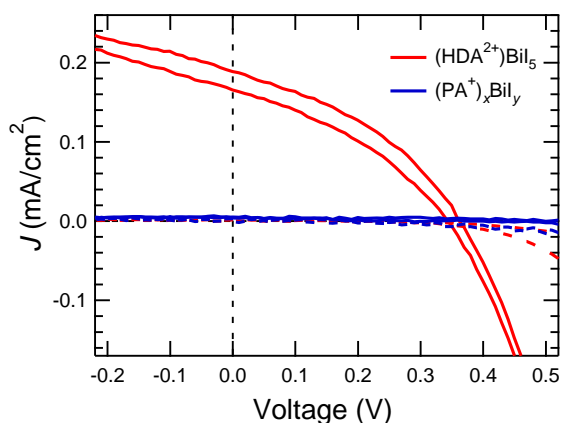


Figure 7. Current density vs. potential data at a scan rate of 100 mV/s for complete solar cells consisting of Au/spiro-OMeTAD/Bi/mTiO₂/ALD-cTiO₂/FTO, where Bi is (HDA²⁺)BiI₅ (red lines) or (PA⁺)_xBiI_y (blue lines), mTiO₂ is mesoporous TiO₂, and ALD-cTiO₂ is atomic-layer-deposited compact TiO₂. Solid lines are from measurements performed under simulated 1 Sun illumination and dashed lines are from measurements performed in the dark.

conversion efficiency of 0.029% (Figure 7, red line). This represents a > 50% increase in J_{SC} compared to our best-performing solar cell that incorporated a solution-deposited cTiO₂ layer.¹¹

Solar cells incorporating (PA⁺)_xBiI_y as the photoactive layer exhibited no appreciable photocurrent (Figure 7, blue line), which is attributed to a combination of inferior zero-dimensional structure of (PA⁺)_xBiI_y in comparison to that of one-dimensional (HDA²⁺)BiI₅ and poor crystallization of (PA⁺)_xBiI_y on the underlying mTiO₂ layer as evidenced by plan-view SEM images (Figure S7c and S7d).

CONCLUSIONS

A comparative study was performed on a hybrid organic–inorganic bismuth–halide material that contained divalent organic cations vs. an analogous material containing monovalent organic cations. The crystal structures of dicationic (HDA²⁺)BiI₅ and monocationic (PA⁺)_xBiI_y

were resolved and shown to differ in that $(\text{HDA}^{2+})\text{BiI}_5$ was orthorhombic and one-dimensional and $(\text{PA}^+)_x\text{BiI}_y$ was triclinic and zero-dimensional. Density functional theory calculations supported experimental absorption data for $(\text{HDA}^{2+})\text{BiI}_5$ and also predicted the bandgap to equal ~ 2 eV. Relationships between structure and material characteristics such as photophysical properties, stability, and film quality were investigated. Appreciable steady-state photoluminescence was observed at room temperature for each of the bismuth–halide materials measured, while a time-resolved photoluminescence signal on the nanosecond and longer timescale was only apparent for $(\text{HDA}^{2+})\text{BiI}_5$ thin films and only when KI was incorporated into the precursor solution. $(\text{HDA}^{2+})\text{BiI}_5$ was shown to be more stable to thermal treatments than $(\text{PA}^+)_x\text{BiI}_y$ and film coverage of $(\text{HDA}^{2+})\text{BiI}_5$ on a TiO_2 -coated FTO substrate was superior to that of $(\text{PA}^+)_x\text{BiI}_y$. Improved film quality and robustness provide rationale for the use of dicationic organic groups as replacements to monocationic organic groups in hybrid organic–inorganic materials. The dicationic materials exhibited photovoltaic action and an open-circuit photovoltage > 350 mV, while the monocationic analogs showed no apparent photoresponse.

ASSOCIATED CONTENT

Supporting Information

The Supporting Information is available free of charge on the ACS Publications website at DOI:

X-ray Data Collection and Structure Solution for $(\text{HDA}^{2+})\text{BiI}_5$ and $(\text{PA}^+)_x\text{BiI}_y$, Structure Solution Definitions, and Density Functional Theory Calculations for $(\text{HDA}^{2+})\text{BiI}_5$, Figures S1–S8, Table S1, and Table S2.

AUTHOR INFORMATION

Corresponding Author

*Email: ardo@uci.edu

Notes

The authors declare no competing financial interest.

ACKNOWLEDGMENTS

D. M. F. and S. A. acknowledge support from the Alfred P. Sloan Foundation under Grant number FG-2017-8888 and the School of Physical Sciences at the University of California Irvine. D. M. F. acknowledges support by the DOE, Office of Science, Office of Workforce Development for Teachers and Scientists, Office of Science Graduate Student Research (SCGSR) program under contract number DE-SC0014664 and by the National Science Foundation Graduate Research Fellowship under Grant number DGE-1321846. D. O. S. acknowledges support from the EPSRC (EP/N01572X/1) and membership of the Materials Design Network. A. M. G. acknowledges Diamond Light Source for the co-sponsorship of a studentship on the EPSRC Centre for Doctoral Training in Molecular Modelling and Materials Science (EP/L015862/1). This work made use of the ARCHER UK National Supercomputing Service (<http://www.archer.ac.uk>), via our membership of the UK's HEC Materials Chemistry Consortium, which is funded by EPSRC (EP/L000202), and the UCL Legion and Grace HPC Facilities. Synchrotron X-ray diffraction was performed on the 11-BM beamline at the Advanced Photon Source at Argonne National Laboratory by beamline staff. Use of the Advanced Photon Source at Argonne National Laboratory was supported by the U. S. Department of Energy, Office of Science, Office of Basic Energy Sciences, under Contract No. DE-AC02-06CH11357. [Scanning electron microscopy and X-ray diffraction work was performed at the UC Irvine Materials Research Institute.](#) The authors thank

Commented [SA7]: Did we use the LSF and need to Ack them? Do we need to provide funding support ack for IMRI, etc.? If not, that's fine, but I just thought that I would check.

Commented [DF8R7]: All the steady-state PL included in this paper was done at NREL, so no.

I have added in the acknowledgment they ask for us to include if the publication relies significantly on IMRI resources. I didn't use either instruments that requires a grant number to be included.

Dr. Qiyin Lin (UC Irvine) for guidance in X-ray diffraction data analysis and Austin Ryan (UC Irvine) for assistance with single-crystal X-ray diffraction data acquisition and analysis.

ABBREVIATIONS

APbX₃, lead-halide-based hybrid organic-inorganic perovskite; (HDA²⁺)BiI₅, hexanediammonium bismuth pentaiodide; (PA⁺)_nBiI_y, propylammonium bismuth iodide; HDAI₂, hexanediamine dihydriodide; PAI, propylamine hydriodide; v/v, volume/volume ratio; DMF, N,N-dimethylformamide; DMSO, dimethylsulfoxide; FTO, fluorine-doped tin-oxide-coated glass; cTiO₂, compact titanium dioxide; mTiO₂, mesoporous titanium dioxide; XRD, X-ray diffraction; SEM, scanning electron microscopy; TGA, thermogravimetric analysis; ALD-cTiO₂, compact [TiO₂-titanium dioxide](#) deposited via atomic layer deposition

REFERENCES

- (1) Mitzi, D. B. Templating and Structural Engineering in Organic-Inorganic Perovskites. *J. Chem. Soc. Dalton Trans.* **2001**, 1–12.
- (2) Liu, D.; Kelly, T. L. Perovskite Solar Cells with a Planar Heterojunction Structure Prepared Using Room-Temperature Solution Processing Techniques. *Nat. Photonics* **2013**, 8, 133–138.
- (3) Giustino, F.; Snaith, H. J. Toward Lead-Free Perovskite Solar Cells. *ACS Energy Letters* **2016**, 1, 1233–1240.
- (4) Green, M. A.; Hishikawa, Y.; Dunlop, E. D.; Levi, D. H.; Hohl-Ebinger, J.; Ho-Baillie, A. W. Y. Solar Cell Efficiency Tables (Version 51). *Prog. Photovoltaics Res. Appl.* **2018**, 26, 3–12.
- (5) Seok, S. I.; Grätzel, M.; Park, N.-G. Methodologies toward Highly Efficient Perovskite Solar Cells. *Small* **2018**, 1704177.

- (6) Crespo-Quesada, M.; Pazos-Outón, L. M.; Warnan, J.; Kuehnel, M. F.; Friend, R. H.; Reisner, E. Metal-Encapsulated Organolead Halide Perovskite Photocathode for Solar-Driven Hydrogen Evolution in Water. *Nat. Commun.* **2016**, *7*, 6–12.
- (7) Chen, Y. S.; Manser, J. S.; Kamat, P. V. All Solution-Processed Lead Halide Perovskite-BiVO₄ Tandem Assembly for Photolytic Solar Fuels Production. *J. Am. Chem. Soc.* **2015**, *137*, 974–981.
- (8) Spurgeon, J. M.; Lewis, N. S. Proton Exchange Membrane Electrolysis Sustained by Water Vapor. *Energy Environ. Sci.* **2011**, *4*, 2993–2998.
- (9) Kumari, S.; Turner White, R.; Kumar, B.; Spurgeon, J. M. Solar Hydrogen Production from Seawater Vapor Electrolysis. *Energy Environ. Sci.* **2016**, *9*, 1725–1733.
- (10) Xiang, C.; Chen, Y.; Lewis, N. S. Modeling an Integrated Photoelectrolysis System Sustained by Water Vapor. *Energy Environ. Sci.* **2013**, *6*, 3713.
- (11) Fabian, D. M.; Ardo, S. Hybrid Organic–Inorganic Solar Cells Based on Bismuth Iodide and 1,6-Hexanediammonium Dication. *J. Mater. Chem. A* **2016**, *4*, 6837–6841.
- (12) Mousdis, G. A.; Papavassiliou, G. C.; Terzis, A.; Raptopoulou, C. P. Preparation, Structures and Optical Properties of HDABiX₅ and HDASbX₅. *Z. Naturforsch.* **1998**, *53b*, 927–931.
- (13) Mitzi, D. B.; Prikas, M. T.; Chondroudis, K. Thin Film Deposition of Organic–Inorganic Hybrid Materials Using a Single Source Thermal Ablation Technique. *Chem. Mater.* **1999**, *11*, 542–544.
- (14) Mitzi, D. B.; Brock, P. Structure and Optical Properties of Several Organic–Inorganic Hybrids Containing Corner-Sharing Chains of Bismuth Iodide Octahedra. *Inorg. Chem.* **2001**, *40*, 2096–2104.
- (15) Mitzi, D. B. Organic–Inorganic Perovskites Containing Trivalent Metal Halide Layers: The Templating Influence of the Organic Cation Layer. *Inorg. Chem.* **2000**, *39*, 6107–6113.

- (16) Sun, S.; Tominaka, S.; Lee, J.-H.; Xie, F.; Bristowe, P. D.; Cheetham, A. K. Synthesis, Crystal Structure, and Properties of a Perovskite-Related Bismuth Phase, $(\text{NH}_4)_3\text{Bi}_2\text{I}_9$. *APL Materials* **2016**, *4*, 031101.
- (17) Li, M. Q.; Hu, Y. Q.; Bi, L. Y.; Zhang, H. L.; Wang, Y.; Zheng, Y. Z. Structure Tunable Organic–Inorganic Bismuth Halides for an Enhanced Two-Dimensional Lead-Free Light-Harvesting Material. *Chem. Mater.* **2017**, *29*, 5463–5467.
- (18) Brandt, R. E.; Kurchin, R. C.; Hoyer, R. L. Z.; Poindexter, J. R.; Wilson, M. W. B.; Sulekar, S.; Lenahan, F.; Yen, P. X. T.; Stevanovic, V.; Nino, J. C.; Bawendi, M. G.; Buonassisi, T. Investigation of Bismuth Triiodide (BiI_3) for Photovoltaic Applications. *J. Phys. Chem. Lett.* **2015**, *6*, 4297–4302.
- (19) Hamdeh, U. H.; Nelson, R. D.; Ryan, B. J.; Bhattacharjee, U.; Petrich, J. W.; Panthani, M. G. Solution-Processed BiI_3 Thin Films for Photovoltaic Applications: Improved Carrier Collection via Solvent Annealing. *Chem. Mater.* **2016**, *28*, 6567–6574.
- (20) Tiwari, D.; Alibhai, D.; Fermin, D. J. Above 600 mV Open Circuit Voltage BiI_3 Solar Cells. *ACS Energy Lett.* **2018**, *3*, 1882-1886.
- (21) Park, B.-W.; Philippe, B.; Zhang, X.; Rensmo, H.; Boschloo, G.; Johansson, E. M. J. Bismuth Based Hybrid Perovskites $\text{A}_3\text{Bi}_2\text{I}_9$ (A: Methylammonium or Cesium) for Solar Cell Application. *Adv. Mater.* **2015**, *27*, 6806–6813.
- (22) Lehner, A. J.; Fabini, D. H.; Evans, H. A.; Hébert, C.-A.; Smock, S. R.; Hu, J.; Wang, H.; Zwanziger, J. W.; Chabynyc, M. L.; Seshadri, R. Crystal and Electronic Structures of Complex Bismuth Iodides $\text{A}_3\text{Bi}_2\text{I}_9$ (A = K, Rb, Cs) Related to Perovskite: Aiding the Rational Design of Photovoltaics. *Chem. Mater.* **2015**, *27*, 7137–7148.

- (23) Huang, X.; Huang, S.; Biswas, P.; Mishra, R. Band Gap Insensitivity to Large Chemical Pressures in Ternary Bismuth Iodides for Photovoltaic Applications. *J. Phys. Chem. C* **2016**, *120*, 28924–28932.
- (24) Kamminga, M. E.; Stroppa, A.; Picozzi, S.; Chislov, M.; Zvereva, I. A.; Baas, J.; Meetsma, A.; Blake, G. R.; Palstra, T. T. M. Polar Nature of $(\text{CH}_3\text{NH}_3)_3\text{Bi}_2\text{I}_9$ Perovskite-Like Hybrids. *Inorg. Chem.* **2017**, *56*, 33–41.
- (25) Zhang, Z.; Li, X.; Xia, X.; Wang, Z.; Huang, Z.; Lei, B.; Gao, Y. High-Quality $(\text{CH}_3\text{NH}_3)_3\text{Bi}_2\text{I}_9$ Film-Based Solar Cells: Pushing Efficiency up to 1.64%. *J. Phys. Chem. Lett.* **2017**, *8*, 4300–4307.
- (26) Kodzasa, T.; Ushijima, H.; Matsuda, H.; Kamata, T. Preparation of Thin Film of Layer Structured Bismuth Iodide with a Long Chain Alkylammonium and Its Nonlinear Optical Property. *Mol. Cryst. Liq. Cryst.* **2000**, *343*, 71–75.
- (27) Hoye, R.; Brandt, R. E.; Osherov, A.; Stevanovic, V.; Stranks, S. D.; Wilson, M. W. B.; Kim, H.; Akey, A. J.; Kurchin, R. C.; Poindexter, J. R.; Wang, E. N.; Bawendi, M. G.; Bulovic, V.; Buonassisi, T. Methylammonium Bismuth Iodide as a Lead-Free, Stable Hybrid Organic-Inorganic Solar Absorber. *Chem. Eur. J.* **2016**, *22*, 2605–2610.
- (28) Scholz, M.; Flender, O.; Oum, K.; Lenzer, T. Pronounced Exciton Dynamics in the Vacancy-Ordered Bismuth Halide Perovskite $(\text{CH}_3\text{NH}_3)_3\text{Bi}_2\text{I}_9$ Observed by Ultrafast UV–Vis–NIR Transient Absorption Spectroscopy. *J. Phys. Chem. C* **2017**, *121*, 12110–12116.
- (29) Kulkarni, A.; Singh, T.; Ikegami, M.; Miyasaka, T. Photovoltaic Enhancement of Bismuth Halide by N-Methyl Pyrrolidone-Assisted Morphology Conversion. *RSC Adv.* **2017**, *7*, 9456–9460.

- (30) Chen, X.; Myung, Y.; Thind, A.; Gao, Z.; Yin, B.; Shen, M.; Cho, S. B.; Cheng, P.; Sadtler, B.; Mishra, R.; Banerjee, P. Atmospheric Pressure Chemical Vapor Deposition of Methylammonium Bismuth Iodide Thin Films. *J. Mater. Chem. A* **2017**, *5*, 24728–24739.
- (31) Papavassiliou, G. C. Three- and Low-Dimensional Inorganic Semiconductors. *Prog. Solid State Chem.* **1997**, *25*, 125–270.
- (32) Misra, R. K.; Cohen, B.-E.; Iagher, L.; Etgar, L. Low Dimensional Organic–Inorganic Halide Perovskite: Structure, Properties, and Applications. *ChemSusChem* **2017**, *10*, 3712–3721.
- (33) Ito, S.; Murakami, T. N.; Comte, P.; Liska, P.; Grätzel, C.; Nazeeruddin, M. K.; Grätzel, M. Fabrication of Thin Film Dye Sensitized Solar Cells with Solar to Electric Power Conversion Efficiency over 10%. *Thin Solid Films* **2008**, *516*, 4613–4619.
- (34) Kim, H.-S.; Lee, C.-R.; Im, J.-H.; Lee, K.-B.; Moehl, T.; Marchioro, A.; Moon, S.-J.; Humphry-Baker, R.; Yum, J.-H.; Moser, J. E.; Grätzel, M.; Park, N.-G. Lead Iodide Perovskite Sensitized All-Solid-State Submicron Thin Film Mesoscopic Solar Cell with Efficiency Exceeding 9%. *Sci. Rep.* **2012**, *2*, 591.
- (35) Xiao, M.; Huang, F.; Huang, W.; Dkhissi, Y.; Zhu, Y.; Etheridge, J.; Gray-Weale, A.; Bach, U.; Cheng, Y.-B.; Spiccia, L. A Fast Deposition-Crystallization Procedure for Highly Efficient Lead Iodide Perovskite Thin-Film Solar Cells. *Angew. Chem. - Int. Ed.* **2014**, *126*, 10056–10061.
- (36) Ulbricht, R.; Hendry, E.; Shan, J.; Heinz, T. F.; Bonn, M. Carrier Dynamics in Semiconductors Studied with Time-Resolved Terahertz Spectroscopy. *Rev. Mod. Phys.* **2011**, *83*, 543–586.
- (37) Lyu, M.; Yun, J. H.; Cai, M.; Jiao, Y.; Bernhardt, P. V.; Zhang, M.; Wang, Q.; Du, A.; Wang, H.; Liu, G.; Wang, L. Organic–Inorganic Bismuth (III)-Based Material: A Lead-Free, Air-Stable

and Solution-Processable Light-Absorber beyond Organolead Perovskites. *Nano Res.* **2016**, *9*, 692–702.

(38) Pazoki, M.; Johansson, M. B.; Zhu, H.; Broqvist, P.; Edvinsson, T.; Boschloo, G.; Johansson, E. M. J. Bismuth Iodide Perovskite Materials for Solar Cell Applications: Electronic Structure, Optical Transitions, and Directional Charge Transport. *J. Phys. Chem. C* **2016**, *120*, 29039–29046.

(39) Ran, C.; Wu, Z.; Xi, J.; Yuan, F.; Dong, H.; Lei, T.; He, X.; Hou, X. Construction of Compact Methylammonium Bismuth Iodide Film Promoting Lead-Free Inverted Planar Heterojunction Organohalide Solar Cells with Open-Circuit Voltage over 0.8 V. *J. Phys. Chem. Lett.* **2017**, *8*, 394–400.

(40) Jain, A.; Voznyy, O.; Sargent, E. H. High-Throughput Screening of Lead-Free Perovskite-like Materials for Optoelectronic Applications. *J. Phys. Chem. C* **2017**, *121*, 7183–7187.

(41) Ganose, A. M.; Savory, C. N.; Scanlon, D. O. Electronic and Defect Properties of $(\text{CH}_3\text{NH}_3)_2\text{Pb}(\text{SCN})_2\text{I}_2$ Analogues for Photovoltaic Applications. *J. Mater. Chem. A* **2017**, *5*, 7845–7853.

(42) Maughan, A. E.; Ganose, A. M.; Candia, A. M.; Granger, J. T.; Scanlon, D. O.; Neilson, J. R. Anharmonicity and Octahedral Tilting in Hybrid Vacancy-Ordered Double Perovskites. *Chem. Mater.* **2018**, *30*, 472–483.

(43) Du, M. H. Efficient Carrier Transport in Halide Perovskites: Theoretical Perspectives. *J. Mater. Chem. A* **2014**, *2*, 9091–9098.

(44) Xiao, Z.; Meng, W.; Wang, J.; Mitzi, D. B.; Yan, Y. Searching for Promising New Perovskite-Based Photovoltaic Absorbers: The Importance of Electronic Dimensionality. *Mater. Horiz.* **2017**, *4*, 206–216.

- (45) Yu, L.; Zunger, A. Identification of Potential Photovoltaic Absorbers Based on First-Principles Spectroscopic Screening of Materials. *Phys. Rev. Lett.* **2012**, 068701.
- (46) Savory, C. N.; Walsh, A.; Scanlon, D. O. Can Pb-Free Halide Double Perovskites Support High-Efficiency Solar Cells? *ACS Energy Lett.* **2016**, 1, 949–955.
- (47) Ganose, A. M.; Savory, C. N.; Scanlon, D. O. Beyond Methylammonium Lead Iodide: Prospects for the Emergent Field of Ns^2 Containing Solar Absorbers. *Chem. Commun.* **2017**, 53, 20–44.
- (48) Stupak, A. P.; Blaudeck, T.; Zenkevich, E. I.; Krause, S.; Von Borczyskowski, C. The Nature of Non-FRET Photoluminescence Quenching in Nanoassemblies from Semiconductor Quantum Dots and Dye Molecules. *Phys. Chem. Chem. Phys.* **2018**, 20, 18579–18600.
- (49) Abdi-Jalebi, M.; Andaji-Garmaroudi, Z.; Cacovich, S.; Stavrakas, C.; Philippe, B.; Richter, J. M.; Alsari, M.; Booker, E. P.; Hutter, E. M.; Pearson, A. J.; Lilliu, S.; Savenije, T. J.; Rensmo, H.; Divitini, G.; Ducati, C.; Friend, R. H.; Stranks, S. D. Maximizing and Stabilizing Luminescence from Halide Perovskites with Potassium Passivation. *Nature* **2018**, 555, 497–501.